

ARTICLE OPEN



Al₂O₃-modified 7YSZ thermal barrier coatings for protection against volcanic ash corrosion

Xiaofeng Zhang¹✉, Xueshi Zhuo^{1,2,3}, Zhengjie Fan^{2,3}, Jie Mao¹, Chunming Deng¹, Changguang Deng¹, Xuesong Mei², Jianlei Cui², Kesong Zhou¹ and Min Liu¹✉

To prevent volcanic ash corrosion using thermal barrier coatings (TBCs), a novel method using Al₂O₃-modification was proposed to reduce molten CMAS wettability on TBCs surface through a lotus effect. Plasma spray-physical vapor deposition (PS-PVD), a third-generation method for TBCs fabrication, was adopted to deposit 7YSZ TBCs with a feather-like microstructure. Then, Al₂O₃ modification was introduced to fabricate a dense Al₂O₃ overlay with nano/micro-sized grains on the TBCs surface. The wetting ability of CMAS on APS/EB-PVD/PS-PVD 7YSZ TBCs was comparatively in situ observed at 1250 °C for 3600 s. The results indicated that the dense Al₂O₃ overlay inhibited penetration of molten CMAS. Additionally, the micro/nano dual-sized structure, which is similar to the papillary structure of a lotus leaf, reduced molten CMAS wettability on the TBCs surface. The results demonstrated that the Al₂O₃-modified TBCs had better CMAS corrosion resistance than the as-deposited APS/EB-PVD/PS-PVD TBCs.

npj Materials Degradation (2022)6:89; <https://doi.org/10.1038/s41529-022-00308-3>

INTRODUCTION

With the rapid increase in global air traffic, the probability of airplanes encountering volcanic ash is on the rise. Generally, the melting point of volcanic ash is lower than 1300 °C^{1,2}. When volcanic ash enters a turbine engine, it passes through the combustion chamber (>2000 °C) of the turbine engine, transforming into molten calcium-magnesium-alumina-silicate (CMAS, CaO-MgO-Al₂O₃-SiO₂, etc.)^{3,4}. A part of the molten CMAS will adhere to the surface of hot components (guide vanes, moving vanes and combustion chamber, etc.), which will lead to premature failure in thermal barrier coatings (TBCs)^{5–7}. Thus, the TBCs that act as protective coatings on hot component surfaces require good CMAS corrosion resistance.

CMAS corrosion is a substantial security challenge for airplanes. In 2010, Iceland's Eyjafjallajökull volcano erupted, sending ash up to 10,000 meters into the sky, which then drifted toward the European continent. Approximately 17,500 flights were deleted per day, which was the first in the history of European air traffic. Due to this major setback, airline operators worldwide lost approximately \$200 million a day. Flying ash in aircraft engines can cause severe damage to hot components or shut them down. In aircraft engines, hot components are generally protected by porous 7YSZ (7–8 wt% Y₂O₃-ZrO₂) TBCs mainly prepared by atmospheric plasma spray (APS), electron beam-physical vapor deposition (EB-PVD) and plasma spray-physical vapor deposition (PS-PVD)^{8–10}. The molten CMAS resulting from volcanic ash can easily infiltrate the porous 7YSZ coating by capillary action, which leads to TBCs spallation due to stiffness degradation as a result of chemical interactions between CMAS and the 7YSZ coating¹¹. In addition, with CMAS corrosion, precipitation of Y-depleted m-ZrO₂ occurs due to the dissolution of metastable tetragonal (t') YSZ grains^{12,13}.

To overcome these challenges associated with volcanic ash corrosion for TBCs, countless approaches have been proposed in the past few decades. It is known that rare-earth pyrochlores and

fluorites (e.g., Gd₂Zr₂O₇, Ti₂AlC, and Hf₆Ta₂O₁₇) are promising TBCs materials^{14–17} that show better CMAS corrosion resistance than 7YSZ. Additionally, doping of more resistant stabilizers (e.g., Al and Ti) in ceramic coatings is also a feasible approach¹⁸. To prevent CMAS infiltration into the porous 7YSZ coating, laser glazing and remelting of the 7YSZ coating to provide a dense layer are typical methods^{19,20}. The aim of the above traditional approaches in the published literature is to hinder the chemical reaction and infiltration of molten CMAS. To expand the scope of potential measures, a simple solution using Al₂O₃-modification technology was proposed to reduce molten CMAS wettability on TBCs surface through a lotus effect. This solution surpasses the effectiveness of traditional methods.

RESULTS AND DISCUSSION

Premature failure analysis of TBCs

Aircraft engines operate in extreme environments, where volcanic ash leading to CMAS corrosion of TBCs is a great challenge, as seen in Fig. 1a. Volcanic ash plumes in the air that are injected into turbine engines can transform into molten CMAS. A portion of the molten CMAS will be deposited on the 7YSZ TBCs surface of turbine vanes (Fig. 1b), leading to premature TBCs failure under the effect of thermochemical and thermomechanical attack. Thermochemical attack results in the dissolution of the desirable tetragonal metastable T' phase due to the depletion of Y₂O₃ and reprecipitation of destabilized ZrO₂ and Zr-bearing particles, depending on the local chemistry of the molten CMAS²¹. The thermomechanical attack is due to the infiltration of molten CMAS into the gaps in the TBCs by capillary forces²². The depth of CMAS infiltration is controlled by fluid properties such as viscosity and surface tension as well as the microstructure of the TBCs. As the CMAS melt flows into the TBCs, it solidifies, thereby filling porous features and producing stiffening of the coating, which leads to a loss of strain tolerance and delamination of the TBCs^{23,24}. For the

¹National Engineering Laboratory for Modern Materials Surface Engineering Technology & The Key Lab of Guangdong for Modern Surface Engineering Technology, Guangdong Institute of New Materials, Guangdong Academy of Sciences, Guangzhou 510650, China. ²State Key Laboratory for Manufacturing Systems Engineering, Xi'an Jiaotong University, Xi'an 710054, China. ³These authors contributed equally: Xueshi Zhuo, Zhengjie Fan. ✉email: zxf200808@126.com; liumin_gz@hotmail.com

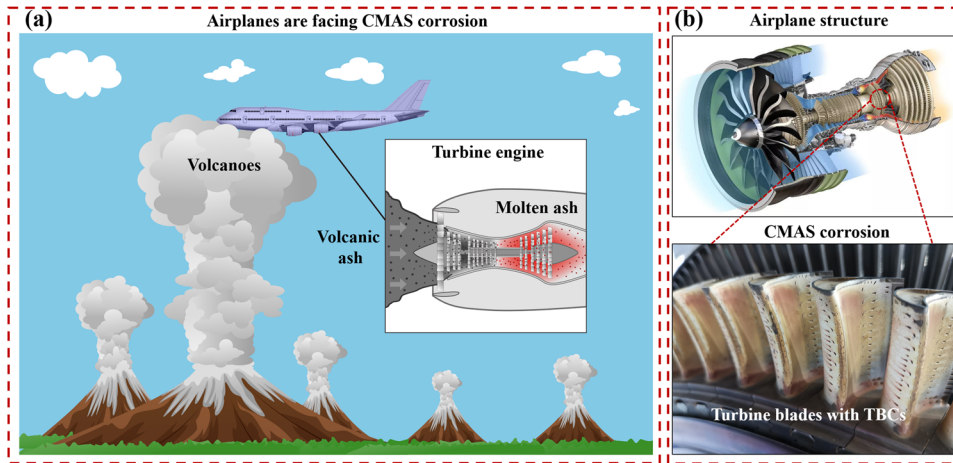


Fig. 1 TBCs in aircraft engines threatened with CMAS corrosion. **a** Volcanic ash in the air from a volcanic eruption. **b** Typical TBCs spallation of moving vanes under CMAS corrosion interactions.

case of initially glassy particles such as many volcanic ashes, a thermomechanical attack can occur at temperatures far below the thermodynamic melting temperature²⁵. Softening and flow of molten ash just above the glass transition temperature are the prevailing mechanisms. With frequent take-offs and landings, TBCs spallation can occur due to chemical and mechanical interactions.

Surface design and realization of 7YSZ TBCs

CMAS corrosion is a major challenge for APS/EB-PVD/PS-PVD 7YSZ TBCs in commercial applications. The lotus effect can overcome this limitation by providing an important solution against volcanic ash corrosion of TBCs. It is known that the hydrophobic performance of lotus leaves is due to the micro/nano dual-sized surface structure. To achieve this effect, a surface design solution involving Al_2O_3 -modification for TBCs was proposed, as shown in Fig. 2. Through this process, the TBCs surface was expected to achieve a lotus leaf structure (Fig. 2a). With this bionic surface structure, the contact area between molten CMAS and TBCs was reduced. Moreover, molten volcanic ash is difficult to spread and infiltrates into the porous 7YSZ coating. Through Al_2O_3 -modification, a dense Al_2O_3 overlay was formed on the TBCs surface, which further hindered CMAS infiltration (Fig. 2b). During the Al_2O_3 -modification process, an Al film with an appropriate thickness was deposited on the 7YSZ TBCs surface. For the Al-deposited TBCs during vacuum heat treatment, the solid state of the Al film changed into a liquid state and infiltrated into TBCs gaps. Additionally, the Al reacted with ZrO_2 forming an $\alpha\text{-Al}_2\text{O}_3$ overlay, which acted as a diffusion barrier for molten CMAS in a high-temperature service environment^{6,26,27}.

Taking PS-PVD as an example, feather-like structured 7YSZ TBCs were obtained by PS-PVD. Vertical gaps of different sizes can be seen throughout the cross-section microstructure (Fig. 3a). After Al film deposition through magnetron sputtering, the 7YSZ coating surface showed a slight change, showing larger-sized Al grains. The cross-section of Al-deposited TBCs indicates that a 5- μm thick layer was deposited on the surface (Fig. 3b). After vacuum heat treatment, further evolution of the TBCs surface occurred. An $\alpha\text{-Al}_2\text{O}_3$ overlay was observed, which resulted from in situ synthesis through Al and ZrO_2 . The formed $\alpha\text{-Al}_2\text{O}_3$ phase was confirmed by XRD and TEM analysis, as shown in Fig. 3c.

Furthermore, the microstructural evolution of the PS-PVD 7YSZ TBCs surface from Al-deposited TBCs to Al_2O_3 -modified TBCs was observed by multifunctional SEM, as shown in Fig. 4. This characterization aimed to elucidate the in situ synthesis of the Al film and the 7YSZ coating. A continuous evolution process for the micro/nano dual-sized surface microstructure was observed.

The surface microstructure of Al-deposited 7YSZ TBCs is shown in Fig. 4a1–a3 with different magnifications for the same area, indicating nano/micro-sized Al grains deposited on the cauliflower-structured surface. The surface microstructure that resulted when the heating temperature was increased to 665 °C is shown in Fig. 4b1–b3. Figure 4b2–b3 show that the Al film melted with a smooth surface. When the temperature was further increased to 810 °C, new grains gradually formed (Fig. 4c1–c3). Next, the heating temperature was increased to 980 °C, and nano/micro-sized grains were observed, showing a micro/nano dual surface (Fig. 4d1–d3). Thus, the results show that a lotus leaf microstructure was obtained through Al_2O_3 -modification.

In situ observation of CMAS on 7YSZ TBCs

The Al_2O_3 -modification solution was used not only for PS-PVD 7YSZ TBCs but also for APS and EB-PVD 7YSZ TBCs. The wetting ability of CMAS on APS/EB-PVD/PS-PVD 7YSZ TBCs was in situ observed, as shown in Fig. 5. A CMAS cylinder sample ($\varnothing 2\text{ mm} \times 2\text{ mm}$) was settled on the TBCs surface in a furnace with heating from 25 to 1250 °C and with a holding time of 3600 s at 1250 °C, as shown in Fig. 5a. Using the above process, the same TBCs sample was tested for two cycles. The wetting abilities of the as-sprayed and Al_2O_3 -modified APS TBCs are shown in Fig. 5b. The results indicate that the contact angle of the as-sprayed APS TBCs (Fig. 5b1) during the first test cycle (14.9°) was larger than that during the second test cycle (10.4°). However, after two cycles, some APS TBCs spallation occurred. Similarly, the contact angle of the Al_2O_3 -modified APS TBCs (Fig. 5b2) during the first test cycle (34.2°) was higher than that during the second test cycle (32.1°). However, after two cycles, no APS TBCs spallation was observed. Through the above comparison analysis, it can be concluded that increasing the number of cycles can lead to contact angle reduction. The Al_2O_3 -modification process has a positive effect on the CMAS corrosion resistance of APS 7YSZ TBCs.

The wetting abilities of the as-deposited and Al_2O_3 -modified EB-PVD 7YSZ TBCs are shown in Fig. 5c. The results indicate that the contact angle of the as-deposited TBCs (Fig. 5c1) during the first test cycle (11.8°) was larger than that during the second test cycle (11.4°) after a holding time of 3600 s at 1250 °C. However, during the first cycle, some TBCs spallation occurred. After the second cycle, the spallation area further expanded. In contrast, after the first and second cycles of testing, no TBCs spallation was observed in the Al_2O_3 -modified EB-PVD 7YSZ TBCs (Fig. 5c2), showing better anti-spallation performance. The contact angle of the Al_2O_3 -modified TBCs during the first cycle of testing (18.5°) was larger than that during the second cycle of testing (10.1°). With

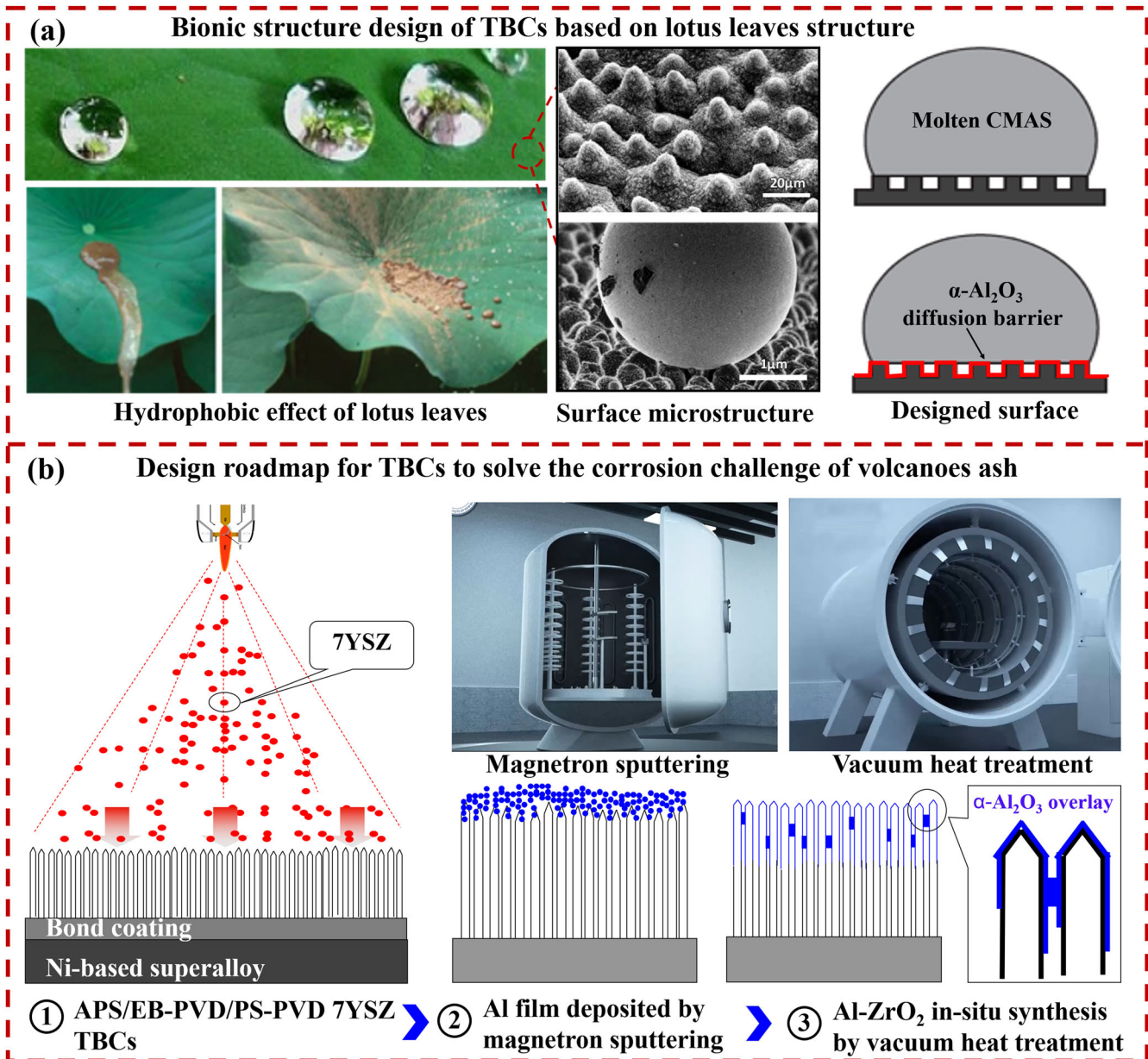


Fig. 2 Surface design of TBCs to prevent CMAS corrosion. **a** Bionic structural design of TBCs based on a lotus leaf structure. **b** Al₂O₃-modification process, including TBCs preparation (APS, EB-PVD, and PS-PVD), Al film deposition by magnetron sputtering, and vacuum heat treatment of Al-deposited TBCs.

increasing numbers of cycles, the contact angle decreased, similar to the APS TBCs. Due to the EB-PVD 7YSZ TBCs has vertical gaps, the molten CMAS can infiltrate into TBCs along the gaps. Through comparison analysis between Fig. 5c1 and c2, it can be concluded that the Al₂O₃-modified 7YSZ TBCs had better CAMS corrosion resistance than the as-deposited EB-PVD TBCs. Thus, using the Al₂O₃-modification process, the corrosion resistance of the EB-PVD TBCs apparently improved, and was equivalent to that of the APS TBCs.

The wetting abilities of the as-sprayed and Al₂O₃-modified PS-PVD TBCs are shown in Fig. 5d. The results indicate that the contact angle of the as-deposited TBCs (Fig. 5d1) during the first test cycle (22.0°) was larger than that during the second test cycle (17.6°) after a holding time of 3600 s at 1250 °C. After two cycles of testing, TBCs spallation occurred. However, the Al₂O₃-modified TBCs (Fig. 5d2) showed no apparent spallation after two cycles of

testing, indicating better anti-spalling ability. The contact angle of the as-deposited TBCs during the first cycle of testing (41.2°) was larger than that during the second cycle of testing (35.7°). By comparing Fig. 5d1 and d2, it can be seen that the CMAS corrosion resistance of PS-PVD 7YSZ TBCs can be improved by means of Al₂O₃-modification. Among Fig. 5b1, c1, d1, the results show that the as-sprayed PS-PVD had better CMAS corrosion resistance than the as-sprayed APS and EB-PVD TBCs (PS-PVD > APS > EB-PVD). Similarly, Fig. (b2, c2, d2) indicate that the Al₂O₃-modified PS-PVD had better CMAS corrosion resistance than the Al₂O₃-modified APS and EB-PVD TBCs (PS-PVD > APS > EB-PVD).

DSC/TG analysis of CMAS powders was carried out, and the analysis showed that CMAS had a low softening point (~700 °C) and low melting temperature (~1080 °C). A contact angle comparison among the APS/EB-PVD/PS-PVD 7YSZ TBCs with and without Al₂O₃-modification is shown in Fig. 6a. The results show

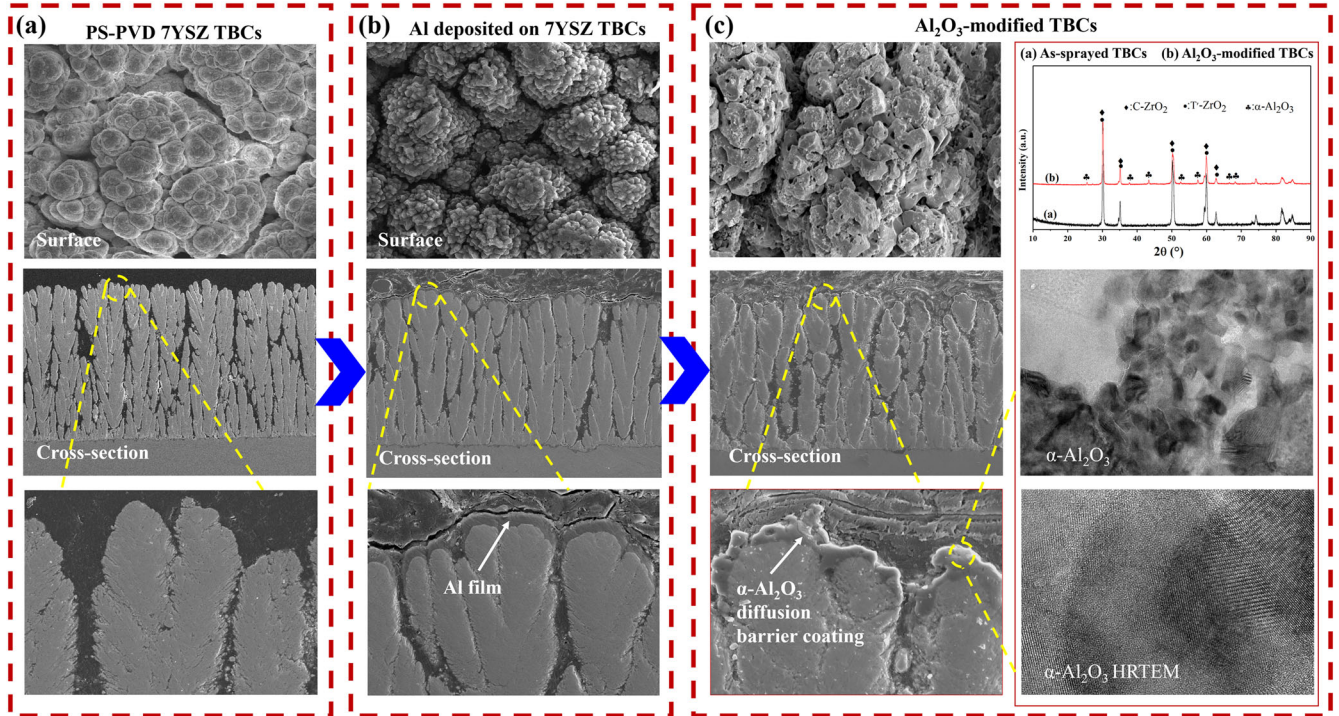


Fig. 3 Microstructural evolution of PS-PVD 7YSZ TBCs during the Al_2O_3 -modification process. **a** Surface and cross-section of as-sprayed TBCs. **b** Surface and cross-section of Al-deposited TBCs. **c** Surface and cross-section of Al_2O_3 -modified TBCs, with XRD and TEM analysis of the Al_2O_3 -modified layer.

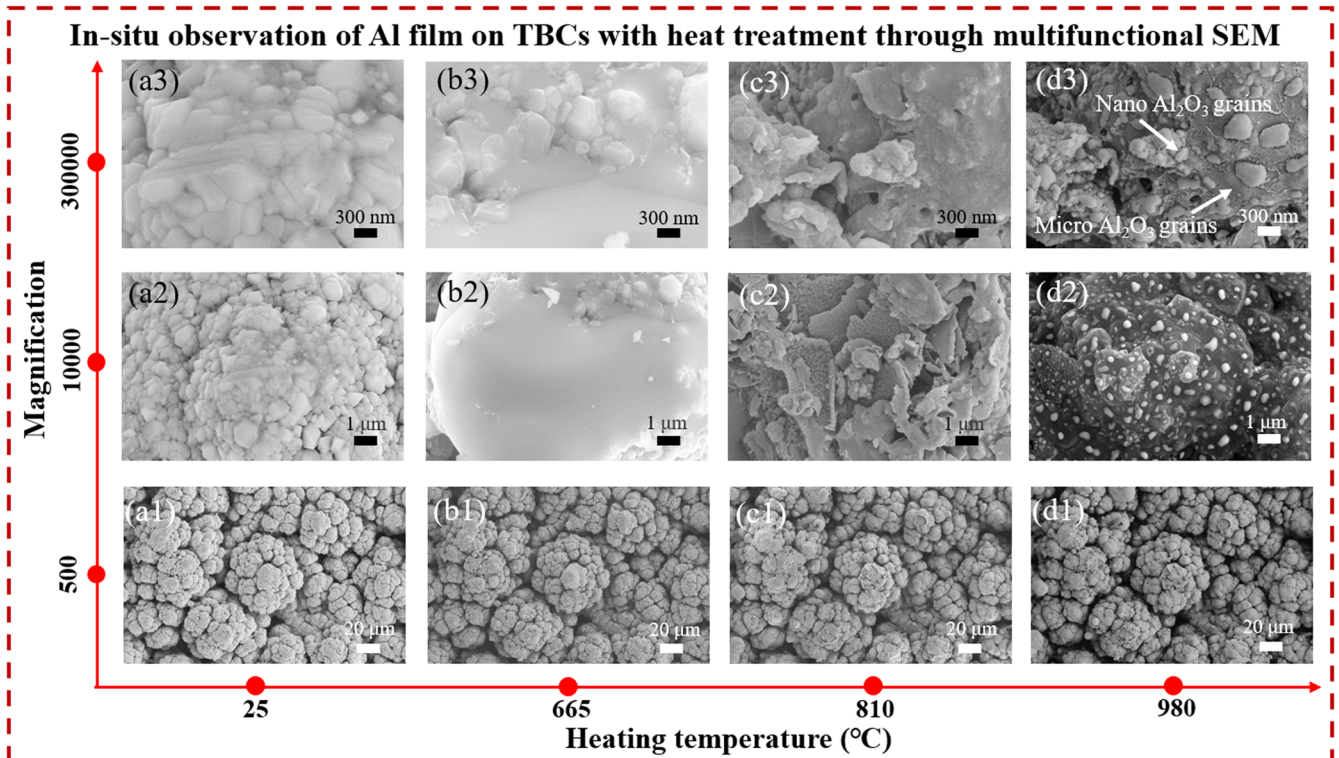


Fig. 4 In situ multifunctional SEM observation of Al film on PS-PVD 7YSZ TBCs with heat treatment. **a1–a3** Surface microstructure at 25 °C. **b1–b3** Surface microstructure at 665 °C. **c1–c3** Surface microstructure at 810 °C. **d1–d3** Surface microstructure at 980 °C.

that the PS-PVD 7YSZ TBCs (with and without Al_2O_3 -modification) had larger contact angles than APS and EB-PVD TBCs (with and without Al_2O_3 -modification). This method for the Al_2O_3 -modification of TBCs is compared with other published literature

methods^{6,26–35}. A wetting angle comparison is presented in Fig. 6b, which shows the largest contact angle after comparison analysis. The contact angle variation with increasing holding time at 1250 °C for APS/EB-PVD/PS-PVD 7YSZ TBCs with and without

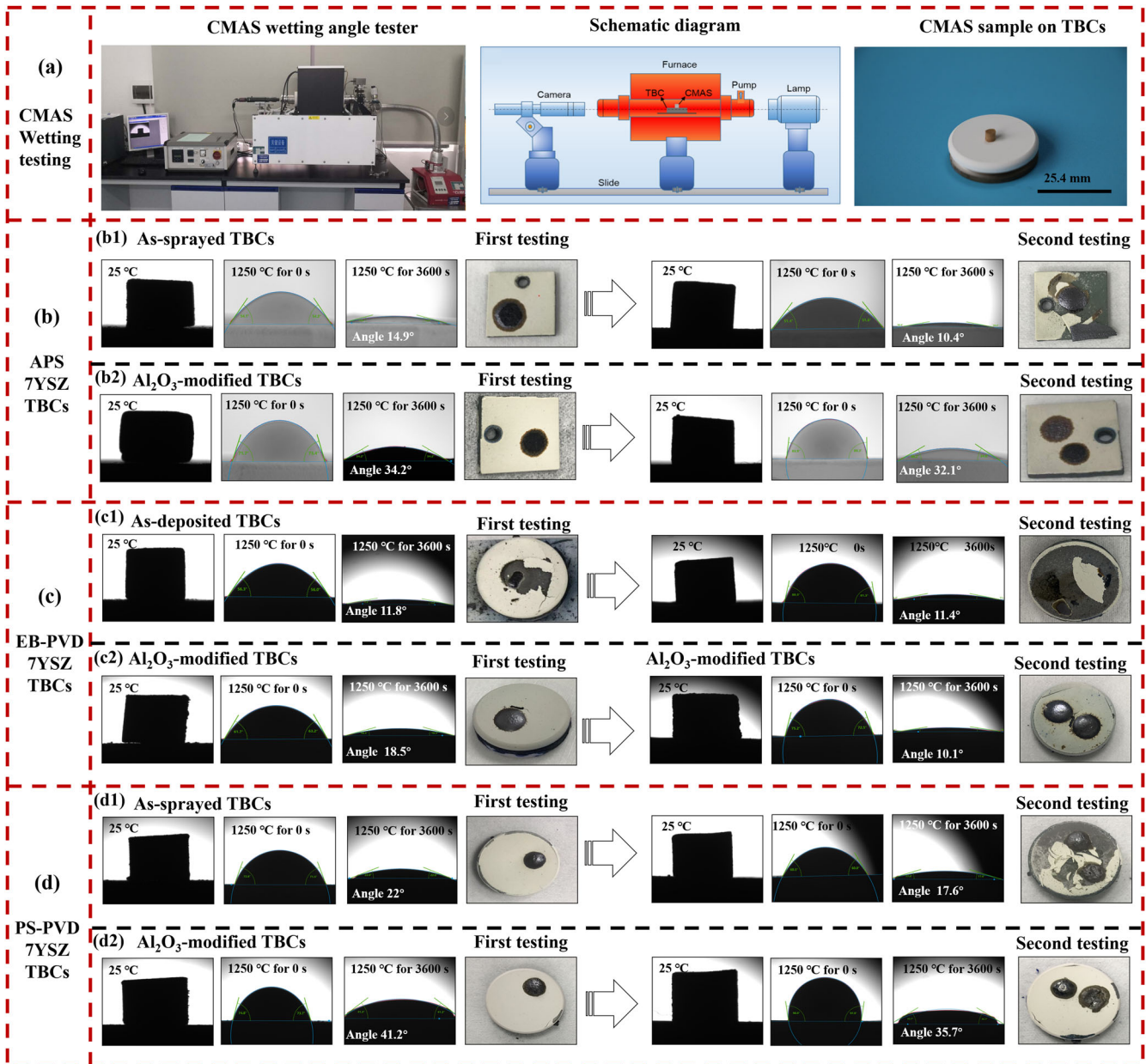


Fig. 5 In situ observed contact angle of CMAS on APS/EB-PVD/PS-PVD 7YSZ TBCs. **a** Testing apparatus and process. **b** As-sprayed and Al₂O₃-modified APS 7YSZ TBCs. **c** As-deposited and Al₂O₃-modified EB-PVD 7YSZ TBCs. **d** As-sprayed and Al₂O₃-modified PS-PVD 7YSZ TBCs.

Al₂O₃-modification is shown in Fig. 6c. The curves show that the contact angle of different TBCs decreased with increasing time, including the time for the heating stage and holding state.

METHODS

TBCs preparation

A NiCrAlY bond coating was prepared on a DZ125 superalloy. The 7YSZ top ceramic coatings were prepared by APS, EB-PVD, and PS-PVD. To further improve their performances, an Al film (5 μm) was deposited on the 7YSZ TBCs surface by magnetron sputtering (J-1250, Jingzhou Industrial Coating, China). Then, the Al-deposited 7YSZ TBCs samples were subjected to vacuum heat treatment to form the Al₂O₃-modified 7YSZ TBCs. During deposition, an Al target (99.99%) was used, and the direct current, voltage, and pressure were set to 3 A, 150 V, and 5 × 10⁻³ Pa, respectively. The

Al-deposited TBCs samples were carried out with vacuum heat treatment at 665, 808, and 980 °C for 1 h at a heating rate of 10 °C/min.

TBCs characterization

The microstructures of the as-sprayed and Al₂O₃-modified 7YSZ TBCs were characterized by field emission-scanning electron microscopy (FE-SEM, Nova-Nano430, FEI) and transmission electron microscopy (TEM, Titan Themis 200, FEI) assisted by focused ion beam (FIB, 450 S, FEI) milling. The phase compositions of the as-sprayed and Al₂O₃-modified TBCs were identified by X-ray diffraction (10–90°, Smart Lab, Rigaku, Japan). The CMAS wettability of the 7YSZ TBCs (APS, EB-PVD, PS-PVD) before and after Al₂O₃-modification was tested by a high-temperature contact angle instrument (DSA30B, KRÜSS, Germany). CMAS samples with

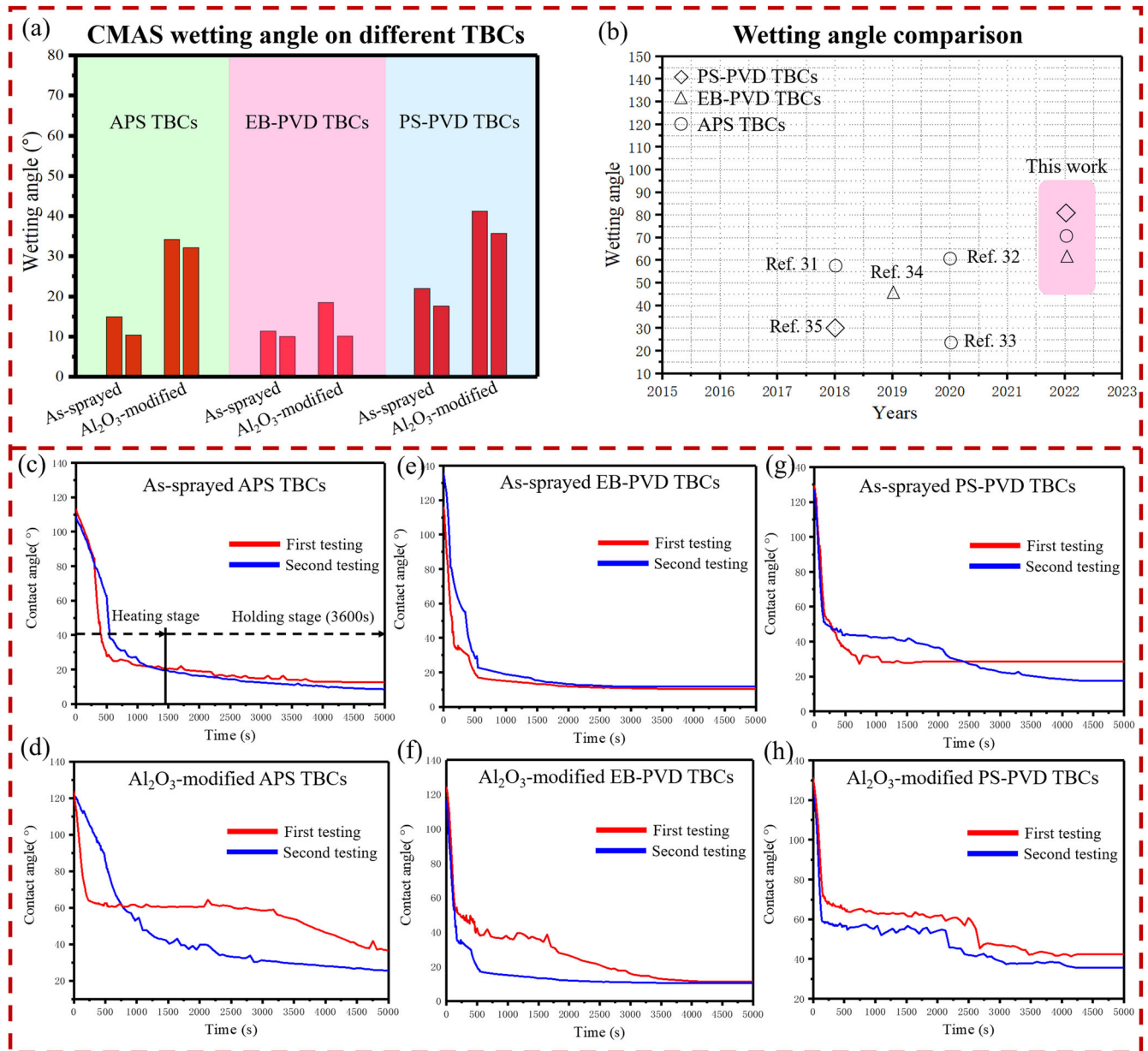


Fig. 6 Comparison of wetting ability of CMAS before and after Al₂O₃-modification in APS/EB-PVD/PS-PVD 7YSZ TBCs. **a** Contact angle comparison among APS/EB-PVD/PS-PVD TBCs. **b** Contact angle comparison with published literature. **c–h** Contact angle variation with increasing time at 1250 °C.

diameters of 2 mm were placed on the TBCs surface and heated to 1250 °C at a rate of ~1 °C/s in an air atmosphere, and the heating temperature was maintained at 1250 °C for 3600 s. During this process, the wetting behavior of the CMAS sample was recorded for a holding time of 3600 s.

DATA AVAILABILITY

The data that support the findings of this study are available from the corresponding author upon reasonable request. Correspondence and requests for materials should be addressed to X.F.Zhang and M.Liu.

Received: 6 September 2022; Accepted: 28 October 2022;
Published online: 10 November 2022

REFERENCES

- Naraparaju, R., Schulz, U., Ramana, C. V. & Gomez, J. Interaction and infiltration behavior of Eyjafjallajökull, Sakurajima volcanic ashes and a synthetic CMAS containing FeO with/in EB-PVD ZrO₂-65 wt%Y₂O₃ coating at high temperature. *Acta Mater.* **136**, 164–180 (2017).
- Fang, H. et al. Investigation of CMAS resistance of sacrificial plasma-sprayed mullite-YSZ protective layer on 8YSZ thermal barrier coating. *Corros. Sci.* **173**, 1–9 (2020).
- Wu, J. et al. Microstructure and thermo-physical properties of yttria stabilized zirconia coatings with CMAS deposits. *J. Eur. Ceram. Soc.* **31**, 1881–1888 (2011).
- Wellman, R. et al. CMAS corrosion of EB PVD TBCs: identifying the minimum level to initiate damage. *Int. J. Refract. Met. Hard Mater.* **28**, 124–132 (2010).
- Zhang, X. et al. In situ synthesis of α -alumina layer on thermal barrier coating for protection against CMAS (CaO–MgO–Al₂O₃–SiO₂) corrosion. *Surf. Coat. Int.* **261**, 54–59 (2015).

6. Zhang, X. et al. Adsorbability and spreadability of calcium-magnesium-alumino-silicate (CMAS) on Al-modified 7YSZ thermal barrier coating. *Ceram. Int.* **42**, 19349–19356 (2016).
7. Morelli, S. et al. CMAS corrosion of YSZ thermal barrier coatings obtained by different thermal spray processes. *J. Eur. Ceram. Soc.* **40**, 4084–4100 (2020).
8. Zhang, X. et al. Tracking the calcium-magnesium-alumino-silicate (CMAS) infiltration into an air-plasma spray thermal barrier coating using X-ray imaging. *Scr. Mater.* **176**, 94–98 (2020).
9. Schulz, U. et al. Effect of processing and interface on the durability of single and bilayer 7YSZ/gadolinium zirconate EB-PVD thermal barrier coatings. *Surf. Coat. Technol.* **381**, 1–10 (2020).
10. Zhang, X. et al. Gas-deposition mechanisms of 7YSZ coating based on plasma spray-physical vapor deposition. *J. Eur. Ceram. Soc.* **36**, 697–703 (2016).
11. Mack, D. et al. Lifetime and failure modes of plasma sprayed thermal barrier coatings in thermal gradient rig tests with simultaneous CMAS injection. *Surf. Coat. Technol.* **324**, 36–47 (2017).
12. Shan, X. et al. Influence of pore characteristics of air plasma sprayed thermal barrier coatings on calcia-magnesia-alumino-silicate (CMAS) attack behavior. *Corros. Sci.* **190**, 1–9 (2021).
13. Li, W. et al. Air plasma-sprayed yttria and yttria-stabilized zirconia thermal barrier coatings subjected to calcium-magnesium-alumino-silicate (CMAS). *J. Therm. Spray. Technol.* **23**, 975–983 (2014).
14. Li, M. et al. Preparation of nanostructured $Gd_2Zr_2O_7-LaPO_4$ thermal barrier coatings and their calcium-magnesium-alumina-silicate (CMAS) resistance. *J. Eur. Ceram. Soc.* **37**, 3425–3434 (2017).
15. Ozgur, Y. et al. Investigation of calcium-magnesium-alumino-silicate (CMAS) resistance and hot corrosion behavior of YSZ and $La_2Zr_2O_7/YSZ$ thermal barrier coatings (TBCs) produced with CGDS method. *Surf. Coat. Technol.* **411**, 1–12 (2021).
16. Yan, Z. et al. Versatility of potential protective layer material Ti_2AlC on resisting CMAS corrosion to thermal barrier coatings. *Corros. Sci.* **167**, 1–14 (2020).
17. Tan, Z. et al. Mechanical properties and calcium-magnesium-alumino-silicate (CMAS) corrosion behavior of a promising $Hf_6Ta_2O_{17}$ ceramic for thermal barrier coatings. *Ceram. Int.* **46**, 25242–25248 (2020).
18. Bilge, S. et al. CMAS-resistant plasma sprayed thermal barrier coatings based on Y_2O_3 -stabilized ZrO_2 with Al^{3+} and Ti^{4+} solute additions. *J. Therm. Spray. Technol.* **23**, 708–715 (2014).
19. Yan, Z. et al. Effects of laser glazing on CMAS corrosion behavior of Y_2O_3 stabilized ZrO_2 thermal barrier coatings. *Corros. Sci.* **157**, 450–461 (2019).
20. Meng, B. et al. Influence of fuel combustion the corrosion behavior of pipeline steels in fire flooding technology. *npj Mater. Degrad.* **21**, 1–9 (2022).
21. Guo, L. et al. Microstructure modification of Y_2O_3 stabilized ZrO_2 thermal barrier coatings by laser glazing and the effects on the hot corrosion resistance. *J. Adv. Ceram.* **9**, 232–242 (2020).
22. Gildersleeve, E. et al. Molten silicate interactions with plasma sprayed thermal barrier coatings: Role of materials and microstructure. *J. Eur. Ceram. Soc.* **39**, 2122–2131 (2019).
23. Liu, Z. et al. Modeling stress evolution in porous ceramics subjected to molten silicate infiltration and corrosion. *Corros. Sci.* **191**, 109698–109698 (2021).
24. Zhou, X. et al. Failure of plasma sprayed nano-zirconia-based thermal barrier coatings exposed to molten $CaO-MgO-Al_2O_3-SiO_2$ deposits. *J. Am. Ceram. Soc.* **102**, 6357–6371 (2019).
25. Jackson, R. et al. Interaction of molten silicates with thermal barrier coatings under temperature gradients. *Acta Mater.* **89**, 396–407 (2015).
26. Zhang, X. et al. Al_2O_3 -modified PS-PVD 7YSZ thermal barrier coatings for advanced gas-turbine engines. *npj Mater. Degrad.* **4**, 1–6 (2020).
27. Song, J. et al. Research of in situ modified PS-PVD thermal barrier coating against CMAS ($CaO-MgO-Al_2O_3-SiO_2$) corrosion. *Ceram. Int.* **42**, 3163–3169 (2016).
28. Wu, X. et al. Microstructure evolution of Al-modified 7YSZ PS-PVD TBCs in thermal cycle. *Ceram. Int.* **47**, 12170–12180 (2021).
29. Zhang, P. et al. Hot corrosion behavior of YSZ thermal barrier coatings modified by laser remelting and Al deposition. *J. Therm. Spray. Technol.* **28**, 1225–1238 (2019).
30. Kang, Y. et al. High temperature wettability between CMAS and YSZ coating with tailored surface microstructures. *Mater. Lett.* **229**, 40–43 (2018).
31. Lokachari, S. et al. Novel thermal barrier coatings with hexagonal boron nitride additives resistant to molten volcanic ash wetting. *Corros. Sci.* **168**, 1–7 (2020).
32. Qu, W. et al. Hot corrosion behavior and wettability of calcium-magnesium-alumina-silicate (CMAS) on $LaTi_2Al_9O_{19}$ ceramic. *Corros. Sci.* **162**, 1–11 (2020).
33. Naraparaju, R. et al. Estimation of CMAS infiltration depth in EB-PVD TBCs: A new constraint model supported with experimental approach. *J. Eur. Ceram. Soc.* **39**, 2936–2945 (2019).
34. Zhang, B. et al. Wetting, infiltration and interaction behavior of CMAS towards columnar YSZ coatings deposited by plasma spray physical vapor. *J. Eur. Ceram. Soc.* **38**, 3564–3572 (2018).
35. Meng, B. et al. On the rumpling mechanism in nanocrystalline coatings: Improved by reactive magnetron sputtering with oxygen. *J. Mater. Sci. Technol.* **132**, 69–80 (2023).

ACKNOWLEDGEMENTS

We would like to acknowledge the financial support from the National Natural Science Foundation of China (51801034 and 52172067), Guangdong Province Outstanding Youth Foundation (2021B1515020038), Guangdong Special Support Program (2019BT02C629), Guangdong Academy of Sciences Program (2020GDASYL-20200104030).

AUTHOR CONTRIBUTIONS

X.F.Z., X.S.Z., and Z.F. conducted experimental studies and analysed the data. J.M., C.M.D., and C.G.D. conducted the TEM experiments. X.M. and J.C. co-wrote the paper. M.L. and K.Z. contributed to the discussion of the results. X.S.Z. and Z.F. are co-first authors of this work.

COMPETING INTERESTS

The authors declare no competing interests.

ADDITIONAL INFORMATION

Supplementary information The online version contains supplementary material available at <https://doi.org/10.1038/s41529-022-00308-3>.

Correspondence and requests for materials should be addressed to Xiaofeng Zhang or Min Liu.

Reprints and permission information is available at <http://www.nature.com/reprints>

Publisher's note Springer Nature remains neutral with regard to jurisdictional claims in published maps and institutional affiliations.



Open Access This article is licensed under a Creative Commons Attribution 4.0 International License, which permits use, sharing, adaptation, distribution and reproduction in any medium or format, as long as you give appropriate credit to the original author(s) and the source, provide a link to the Creative Commons license, and indicate if changes were made. The images or other third party material in this article are included in the article's Creative Commons license, unless indicated otherwise in a credit line to the material. If material is not included in the article's Creative Commons license and your intended use is not permitted by statutory regulation or exceeds the permitted use, you will need to obtain permission directly from the copyright holder. To view a copy of this license, visit <http://creativecommons.org/licenses/by/4.0/>.

© The Author(s) 2022